nature climate change

Article

https://doi.org/10.1038/s41558-024-02136-6

Climate variability shifts the vertical structure of phytoplankton in the Sargasso Sea

Received: 20 December 2023

Accepted: 22 August 2024

Published online: 25 September 2024

Check for updates

Johannes J. Viljoen ✉, Xuerong Sun & Robert J. W. Brewin

Marine phytoplankton are essential to ocean biogeochemical cycles. However, our understanding of changes in phytoplankton rely largely on satellite data, which can only assess changes in surface phytoplankton. How climate variability is impacting their vertical structure remains unclear. Here we use 33 years' worth of data from the Sargasso Sea to show distinct seasonal and long-term phytoplankton climate responses in the surface mixed layer compared with the subsurface. Seasonally, the surface community alters their carbon-to-chlorophyll ratio without changing their carbon biomass, whereas the chlorophyll *a* and carbon of the subsurface community covaries with no change in their carbon-to-chlorophyll ratio. Over the last decade, the subsurface phytoplankton biomass has increased in response to warming, whereas the surface phytoplankton have altered their carbon-to-chlorophyll ratio with minimal change in their carbon biomass. Given that satellites can only view the surface ocean, sustained subsurface monitoring is required to provide a full understanding of how phytoplankton are responding to climate change.

Marine phytoplankton are photosynthetic, single-celled microscopic organisms that form the base of the marine food-web[1,2]. They are essential in the regulation of global ocean biogeochemical cycles and climate[3,4]. Physical and chemical changes in the ocean are modifying the distribution, phenology, abundance and composition of phytoplankton, impacting higher trophic levels and biological carbon export[5,6]. Improving our understanding of the impact of upper-ocean warming, and concurrent increased stratification, on phytoplankton is critical to predicting changes in planetary biogeochemical cycles and the marine ecosystem[7–11].

Global estimates of phytoplankton abundance are often acquired using the satellite remote sensing of ocean colour, due to its unparalleled capability of observing the surface ocean at high spatial and temporal resolutions[12]. However, satellite ocean colour observations can only monitor surface phytoplankton communities (<50 m depth in the clearest waters[13]). Below the surface mixed layer of the seasonally and permanently stratified regions, which cover more than 70% of the global ocean, resides an understudied subsurface community that satellites cannot see[14,15]. This community can contribute a substantial portion of the total water-column phytoplankton biomass and production[16–19] and can have contrasting phenology to surface communities[20,21]. Subsurface phytoplankton often form deep chlorophyll maximums (DCM) or subsurface chlorophyll maximums (SCM)[15], and blooms often occurring for longer periods than in surface communities[22]. Considering the relevance of subsurface communities, it is essential to improve our understanding of how phytoplankton vertical structure may be impacted by upper-ocean warming and stratification as a result of climate variability.

The increasing wealth of data provided by autonomous platforms, such as Biogeochemical-Argo floats, can complement satellite data and improve our ability to monitor phytoplankton at depth[15,21]. Recently, a model was developed to partition the vertical structure of phytoplankton biomass into two communities—a surface community visible by satellite and a subsurface community below the

Centre for Geography and Environmental Science, Department of Earth and Environmental Sciences, Faculty of Environment, Science and Economy, University of Exeter, Cornwall, UK. ✉e-mail: j.j.viljoen@exeter.ac.uk

https://doi.org/10.1038/s41558-024-02136-6

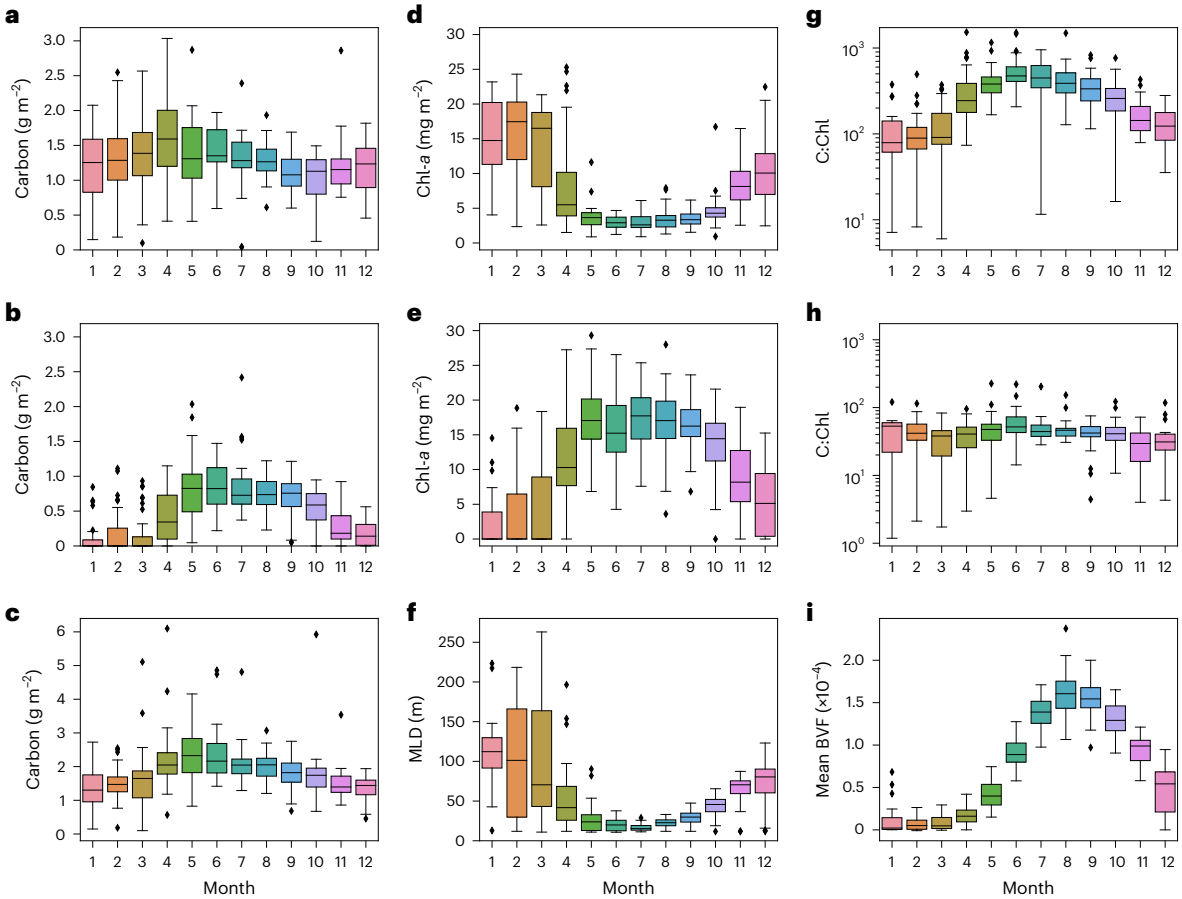

Fig. 1 | Seasonality in surface and subsurface phytoplankton from BATS. **a**–**c**, Monthly boxplots of surface (**a**), subsurface (**b**) and total (**c**) phytoplankton carbon integrated concentrations. **d**,**e**, Surface (**d**) and subsurface (**e**) Chl-*a* integrated stocks. **f**, MLD. **g**,**h**, Surface (**g**) and subsurface (**h**) phytoplankton C:Chl ratios. **i**, Mean Brunt–Väisälä buoyancy frequency (BVF) stratification index. In all panels, the centre line is the median, boxes represent the interquartile range (25th to 75th percentiles), whiskers 1.5× interquartile range and diamond points are the outliers beyond this range. See Methods for details on the computation of the MLD, BVF and column integrations. Depth integration was done from the surface to 1.5 times the euphotic depth (1.5× Z_p) (Methods). See Extended Data Fig. 1 for monthly boxplots based on concentrations instead of integrated stocks, which reveal similar seasonal cycles. See Extended Data Figs. 7 and 9 for the entire time series for MLD, mean BVF, integrated Chl-*a* and POC model results, and C:Chl ratios. See Supplementary Table 3 for the number of profiles and values per month used to calculate each boxplot.

mixed layer—hidden from satellite observation[20]. This tool has been combined with Biogeochemical-Argo data to observe phytoplankton biomass dynamics below the mixed layer[19,20]. However, because these platforms are relatively recent additions to the ocean observing system, they have not yet yielded the long-term records that ship-based observations provide[23]. Although ship-based surveys provide limited spatial coverage, they can provide long-term, frequent and high-quality observations of phytoplankton vertical structure at specific sites, such as the seasonally stratified Bermuda Atlantic Time-series Study (BATS) site in the Sargasso Sea (see Supplementary Section 3 for further details about the site), making them suitable for observing longer-term trends in subsurface phytoplankton. Recent studies at BATS have shown that ocean warming is linked to a long-term decline in phytoplankton productivity and adaption in carbon export strategies due to increased water-column stratification[24,25].

Here we apply a conceptual model[20] to in situ ship-based data from BATS to explore the phytoplankton dynamics of two communities (surface and subsurface) over a 33-year period (1990–2022). The surface community is reflective, primarily, of the phytoplankton in the mixed layer (a turbulent environment with variable light), with the subsurface community reflecting the phytoplankton below the mixed layer (a low-light environment)[20]. BATS provides a unique opportunity to explore the effects of warming and mixed-layer dynamics on the vertical distribution of phytoplankton biomass due to its multidecadal record of measured vertical profiles of chlorophyll *a* (Chl-*a*) concentrations and particulate organic carbon (POC)[26], which are converted here to estimates of phytoplankton-specific biomass. The model is used to interpolate (or extrapolate) sparse observations over the water column, capturing features of the profile, and to intuitively estimate phytoplankton carbon from POC profiles (see Supplementary Section 4.3). We infer the portions of Chl-*a* and POC contributed by the surface and subsurface communities separately (Methods and Supplementary Information), and study the seasonality and multidecadal trends in the carbon-to-Chl-*a* ratios (C:Chl) of the two communities. BATS is ideal for this type of analysis because of its location, dataset length (33 years, 1990–2022), conditions and similarity to other subtropical ocean regions[26]. Our results suggest upper-ocean warming is impacting the vertical structure of phytoplankton in seasonally stratified regions and point to a need for improved monitoring at depths below satellite observational capabilities.

Seasonal contrasts in surface and subsurface phytoplankton

Surface phytoplankton carbon integrated stocks (Fig. 1a) and concentrations (Extended Data Fig. 1a) remain relatively stable over the season, whereas subsurface phytoplankton carbon shows a clear seasonal

https://doi.org/10.1038/s41558-024-02136-6

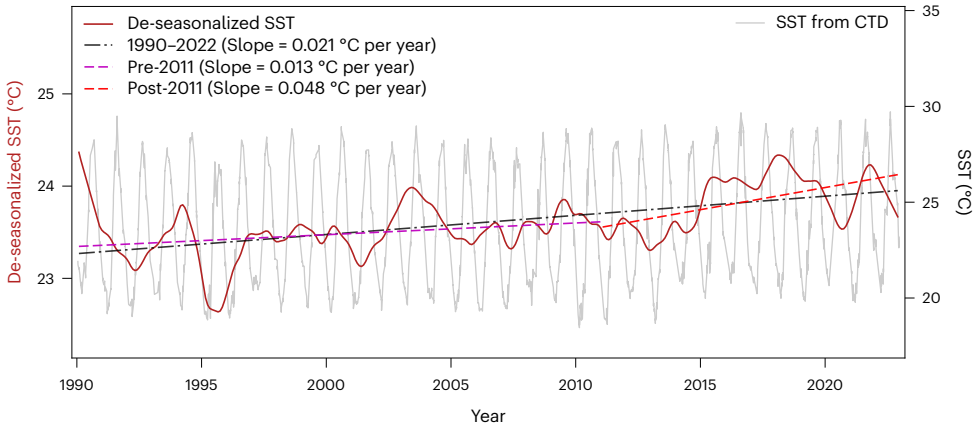

Fig. 2 | Multidecadal increasing surface-ocean temperature trend from BATS and how it changed over the last 12 years. Time series of SSTs taken as the median in the upper 11 m of the water column. Solid grey line, SSTs from the BATS CTD profiles used in the study; solid red line, de-seasonalized SST data; dashed black line, linear regression applied to the entire de-seasonalized SST time series (1990–2022); dashed purple line, linear regression fitted to de-seasonalized SSTs to the end of 2010 (pre-2011 includes 1990–2010); dashed red line, linear regressions fitted to the de-seasonalized SSTs from 2011 to the end of 2022 (post 2011 includes 2011–2022). All trends were significant (Pearson correlation, $P = 0$). See Data analysis for extraction of the de-seasonalized data and for details on the linear trend analysis (Methods).

cycle with the highest (lowest) stocks and concentrations occurring in the summer (winter) (Fig. 1b and Extended Data Fig. 1b). This seasonal signature in the subsurface is reflected in the total vertically integrated phytoplankton carbon (Fig. 1c). In winter, a deeper mixed layer (Fig. 1f) and lower solar irradiance means there is not sufficient light below the mixed layer for the subsurface community to maintain high concentrations (Fig. 1b). By contrast, in the summer, following the onset of stratification (Fig. 1i), the mixed layer is shallower (Fig. 1f) and the irradiance higher (Extended Data Fig. 2e,f), meaning there is sufficient light below the mixed layer for the subsurface community to grow (Fig. 1b). Irradiance levels at the DCM suggest that the subsurface community is predominantly light-limited over the time series (Extended Data Fig. 3c). Subsurface phytoplankton are unlikely to be limited by nutrients due to their access to deeper, nutrient-rich waters, with nitrate concentrations notably higher below the mixed layer (Extended Data Fig. 3b). This is also supported by BATS observations of particulate stoichiometric ratios that suggest the base of the euphotic zone may be less nutrient stressed[24]. Top-down control (for example, grazing) also plays a critical role in controlling phytoplankton biomass in the subsurface (for example, ref. 27).

In contrast to the surface phytoplankton carbon (Fig. 1a), surface Chl-*a* integrated stocks (Fig. 1d) and concentrations (Extended Data Fig. 1c) show a marked seasonality, with the highest (lowest) stocks occurring in winter (summer). Seasonality in the C:Chl ratio of the surface community (Fig. 1g) indicates it is controlled by photoacclimation and/or shifts in the taxonomic structure (Extended Data Figs. 4 and 5)[24,28–30], with the surface community decreasing (increasing) its Chl-*a*, per unit carbon, in the higher (lower) mixed-layer irradiance (Extended Data Figs. 2e and 6a) during summer (winter). Alternatively, the seasonality in the subsurface Chl-*a* (Fig. 1e) is consistent with that of the subsurface phytoplankton carbon (Fig. 1b), with no evident changes in their C:Chl ratio over the seasons (Fig. 1h). This indicates that the subsurface community maintains a stable C:Chl ratio at the seasonal scale (permanently adapted to low light conditions, with a lower C:Chl ratio when compared with the surface phytoplankton community) (Supplementary Table 1), possibly due to longer-term acclimation to low light conditions[18,31].

Long-term trends and ocean warming

The time series of surface-ocean temperature (median in the upper 11 m) from the conductivity, temperature and depth (CTD) sensor data included in this study (1990–2022) shows a significant increasing trend over the entire time series (slope = 0.021 °C yr^{-1}, $P < 0.001$) (Fig. 2). This increasing trend corresponds to an increase of about 0.7 °C over 33 years, which is similar to that reported in a recent BATS study (1990–2020)[24].

Persistent ocean warming and weakened vertical mixing at the BATS site have previously been linked to reduced primary productivity[25] and changes in carbon export of phytoplankton[24]. The de-seasonalized integrated Chl-*a* showed a weak positive trend (1990–2022, slope = 0.024 mg m^{-2} yr^{-1}, $P < 0.05$) (Fig. 3a). However, differences are seen when the surface and subsurface communities are studied separately (Fig. 3b,c). The surface Chl-*a* showed no significant trend, while the subsurface Chl-*a* increased (slope = 0.024 mg $m^{-2}yr^{-1}$, $P < 0.01$) (Fig. 3c). In contrast to Chl-*a*, the total phytoplankton carbon decreased weakly (slope = −0.002 g $m^{-2}yr^{-1}$, $P = 0.05$) (Fig. 3e). However, this decrease appears to be due to a decrease in surface phytoplankton carbon (slope = −0.002 g $m^{-2}yr^{-1}$, $P < 0.05$) (Fig. 3f), with subsurface phytoplankton carbon showing no significant trend (Fig. 3g). The surface C:Chl ratio decreased weakly (slope = −0.998 per year, $P < 0.05$) (Fig. 3d), although there was a very significant decreasing trend in the subsurface C:Chl ratio (slope = −0.2 per year, $P < 0.001$) (Fig. 3h). Overall, these results illustrate the two communities respond to longer-term climate trends differently.

Lomas et al.[24] identified a shallowing of the winter maximum mixed-layer depth (MLD) in the 2010s. This decreasing trend in the depth of winter mixing occurred after an anomalous maximum deep winter MLD in 2010, linked to an unusual winter North Atlantic Oscillation index and an eddy event[24,26,32]. Our analysis of MLDs at BATS also revealed this maximum MLD during the winter of 2010, after which the winter maximum MLD steadily decreased (Extended Data Fig. 7d). Following Lomas et al.[24], we partitioned our time series into pre-2011 and post-2011, the selected change point supported by two objective techniques (Methods). Our trend analysis of de-seasonalized sea-surface temperatures (SSTs) (Fig. 2) and de-seasonalized MLD data (Extended Data Fig. 8) also showed stark changes after 2010, with stronger increasing SST and decreasing MLD trends (that is, a significant shallowing trend) compared with previous years. Closer analysis of the time series indicated that, before 2011 (1990–2010), the integrated total Chl-*a* was increasing significantly (slope = 0.169 mg $m^{-2}yr^{-1}$, $P < 0.001$) (Fig. 3a), in line with increases in the surface Chl-*a* (slope = 0.164 mg $m^{-2}yr^{-1}$, $P < 0.001$) (Fig. 3b). Contrastingly, the integrated total carbon was decreasing significantly (slope = −0.008 g $m^{-2}yr^{-1}$, $P < 0.001$) (Fig. 3e), but this decrease can be attributed to the subsurface (slope = −0.008 g $m^{-2}yr^{-1}$,

https://doi.org/10.1038/s41558-024-02136-6

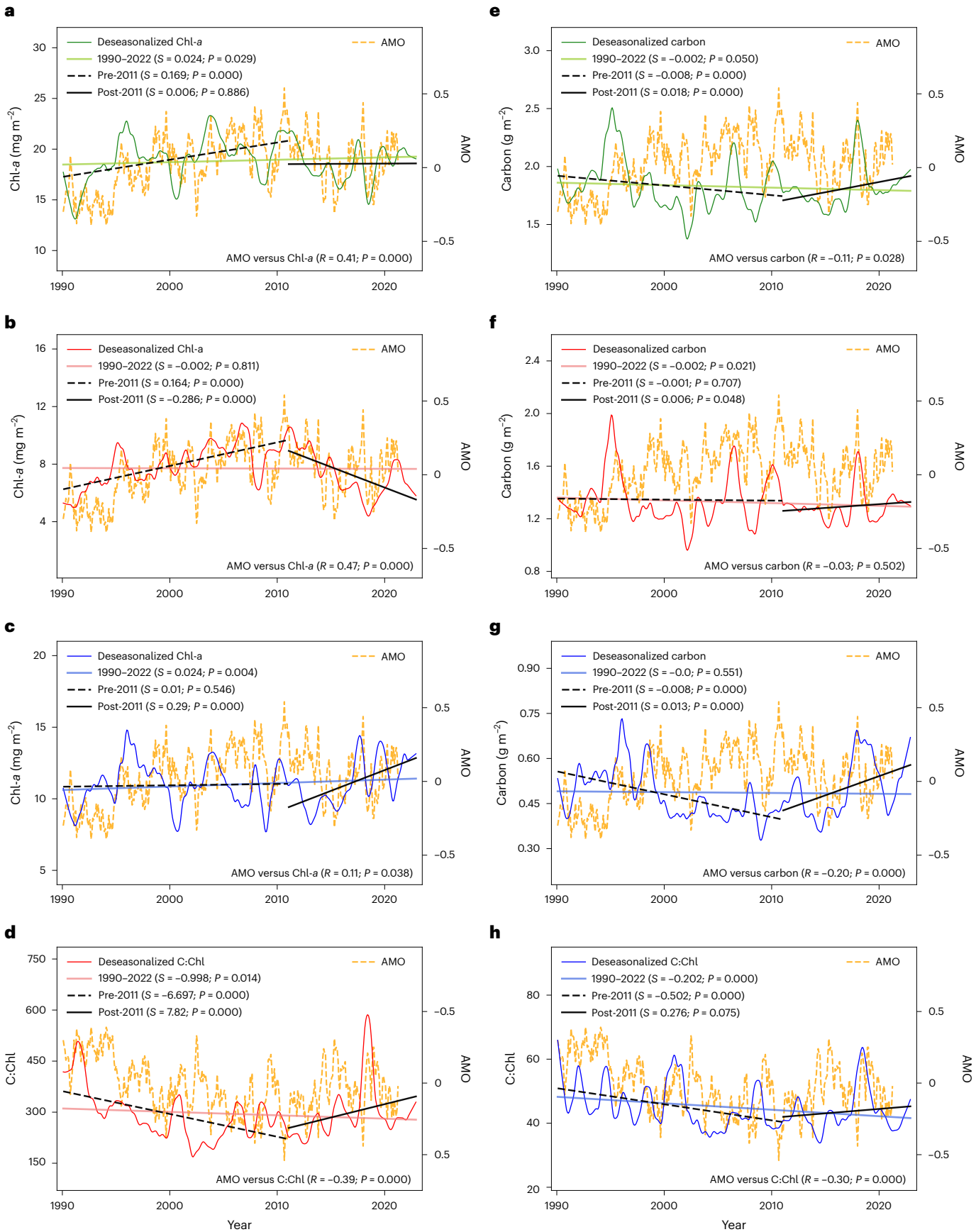

Fig. 3 | Multidecadal trends in surface and subsurface chlorophyll and phytoplankton carbon with links to climate variability. a–**c**, Time series of de-seasonalized integrated Chl-*a* for total modelled Chl-*a* (**a**), surface Chl-*a* (**b**) and subsurface Chl-*a* (**c**). **d**,**h**, Modelled C:Chl ratio for surface (**d**) and subsurface (**h**) communities. **e**–**g**, Integrated phytoplankton carbon: total modelled phytoplankton carbon (**e**), surface carbon (**f**) and subsurface carbon (**g**). The de-seasonalized data were extracted from column-integrated ($1.5\times Z_p$) concentrations (Methods). Light coloured lines, linear regression fitted to the entire time series (1990–2022); thick dashed black lines, linear regressions fitted to de-seasonalized data to the end of 2010 (pre-2011 includes 1990–2010); thick solid black lines, linear regressions fitted to de-seasonalized data only from 2011 to the end of 2022 (post 2011 includes 2011–2022); *S*, slope of the trend; and *P*, significance of the trend from Pearson correlation; yellow dashed lines, monthly AMO index to March 2021 from the National Center for Atmospheric Research (Data Availability) with Spearman correlation coefficient (*R*) and significance (*P*) of the correlation with the de-seasonalized data. See Supplementary Fig. 1 for cumulative Chl-*a* anomalies superimposed on cumulative AMO, showing a similarly strong relationship between surface Chl-*a* and the AMO index. See Supplementary Fig. 2 for cumulative C:Chl ratio anomalies superimposed on cumulative AMO, illustrating similar relationships with the AMO index. See Supplementary Fig. 3 for a similar trend analysis based on concentrations instead of integrated stocks.

$P < 0.001$) (Fig. 3g), with no significant change in the surface carbon (slope = −0.001 g $m^{-2} yr^{-1}$, $P = 0.707$) (Fig. 3f). Post 2011 (2011–2022), these trends changed (Fig. 3).

Recent warming increased subsurface phytoplankton biomass

The period 2011 to 2022 was characterized by rapid warming and increased stratification[24]. During this period, the SST showed an increasing trend threefold greater than in previous years (1990–2010) that corresponded to an increase of around 0.6 °C in just 12 years (2011–2022) (Fig. 2). Here we identified a decade-scale shift in the phytoplankton vertical structure (Fig. 3). Despite no noticeable trends in the total Chl-*a* (Fig. 3a), the surface Chl-*a* decreased strongly from 2011 to 2022 (slope = −0.286 mg $m^{-2} yr^{-1}$, $P < 0.001$) (Fig. 3b) and the subsurface Chl-*a* increased (slope = 0.29 mg $m^{-2} yr^{-1}$, $P < 0.001$) (Fig. 3c). Contrastingly, the total phytoplankton carbon increased during this period (slope = 0.018 g $m^{-2} yr^{-1}$, $P < 0.001$) (Fig. 3e), mostly driven by an increase in subsurface phytoplankton carbon (slope = 0.013 g $m^{-2} yr^{-1}$, $P < 0.001$) (Fig. 3g), with minimal change in surface phytoplankton carbon (Fig. 3f).

Our results suggest that, in the last decade, the subsurface phytoplankton biomass became decoupled from the surface community in response to rapid warming and increased stratification. During this rapid warming period, surface phytoplankton responded by modifying their physiology or taxonomic composition (the C:Chl ratios of the surface community increased after 2011; slope = 7.82 per year, $P < 0.001$) (Fig. 3d) while maintaining a somewhat stable carbon biomass. Both photoacclimation and community composition could have contributed to the increasing surface C:Chl, as suggested by a significant relationship between surface C:Chl and both community composition (Extended Data Fig. 5a,b) and mixed-layer irradiance (Extended Data Fig. 6a). By contrast, the subsurface community showed a strong biomass increase (both in Chl-*a* and carbon), with no significant trend in the subsurface C:Chl ratios (Fig. 3h).

Climate variability shifts phytoplankton vertical structure

In the context of climate change and ocean warming, it is essential to also consider the influence of multidecadal climate variability in the North Atlantic on phytoplankton biomass. The Atlantic Multidecadal Oscillation (AMO) index (also referred to as 'Atlantic Multidecadal Variability'), based on SST changes, is a useful metric of North Atlantic climate variability[33–35]. Here we investigated the relationship between the monthly AMO index[36] and the de-seasonalized integrated surface and subsurface phytoplankton Chl-*a*, carbon and C:Chl ratios using Spearman correlation analysis.

The de-seasonalized total integrated Chl-*a* (Fig. 3a), up to the end of the available AMO index (that is, March 2021), significantly correlated with the monthly AMO index ($R = 0.41$, $P < 0.001$) (Fig. 3a). However, closer analysis of the de-seasonalized surface and subsurface Chl-*a* revealed that this significant correlation was mostly due to the surface community ($R = 0.47$, $P < 0.001$) (Fig. 3b), with the subsurface Chl-*a* showing a very weak relationship with the AMO (Fig. 3c). The surface phytoplankton carbon showed no significant relationship with the AMO (Fig. 3f), and the subsurface carbon was only weakly correlated ($R = -0.20$, $P < 0.001$) (Fig. 3g). The physiology (C:Chl ratio) of the surface community also correlated better with the AMO ($R = -0.39$, $P < 0.001$) (Fig. 3d) than the subsurface community ($R = -0.30$, $P < 0.001$) (Fig. 3h). Similar results were found when studying the concentrations of these two communities (Supplementary Fig. 3). The results suggest surface phytoplankton in the Sargasso Sea respond to climate variability by adjusting their C:Chl ratio[10], whereas subsurface phytoplankton show some evidence of responding with a change in biomass (Fig. 3g). Interestingly, a cumulative subsurface C:Chl anomaly (Supplementary Fig. 2b) indicates a temporal offset in the response of the subsurface to climate forcing at the surface (AMO). Closer analysis using lag correlation revealed that the relationship between the AMO and subsurface Chl-*a* (Supplementary Fig. 4a) becomes significantly negative with a maximum correlation ($R = -0.34$) after a temporal offset of 2 years, and the already significant relationship with subsurface carbon becomes even stronger (up to $R = -0.52$) (Supplementary Fig. 4b).

Implications for monitoring phytoplankton biomass

Our results suggest that the surface and subsurface communities respond differently to physical changes in the water-column structure caused by climate variability and ocean warming. At present, our best tool for monitoring phytoplankton biomass globally is through satellite observations of ocean colour[37]. However, satellite observations are only capable of viewing the surface community[20]. Assessments of the response of phytoplankton to climate variability and ocean warming, based solely on satellite observations (for example, ref. 38), do not consider that the subsurface community may respond differently to environmental change. To get the full picture of how the phytoplankton are responding to climate variability, we need sustained and systematic observations of the subsurface. At present, this can only be achieved through the continued support of long-term oceanographic stations, such as BATS, and by expanding the network of autonomous platforms that can monitor the vertical structure of phytoplankton at global scales[39–43]. Developments in the use of satellite active light detection and ranging (lidar) data for the global profiling of ocean plankton populations may also play an important role[44].

Our results indicate that the understudied subsurface community, situated below the mixed layer and hidden from satellite view, is important in controlling the variability of column-integrated phytoplankton carbon in regions such as the Sargasso Sea. This subsurface community is also supported by new nutrients entering the system and may contribute considerably to increased productivity and export production[18,45]. Considering its position in the water column, spatially closer to the daily vertical migrations of zooplankton, this subsurface community may sustain different trophic pathways in the marine ecosystem than that of the community in the surface mixed layer, with implications for secondary production, trophic energy transfer and fisheries. It is essential to study this community in more detail if we are to improve our understanding of ocean biogeochemical cycles and climate change.

Online content

Any methods, additional references, Nature Portfolio reporting summaries, source data, extended data, supplementary information, acknowledgements, peer review information; details of author contributions and competing interests; and statements of data and code availability are available at https://doi.org/10.1038/s41558-024-02136-6.

References

1. Falkowski, P. G., Barber, R. T. & Smetacek, V. Biogeochemical controls and feedbacks on ocean primary production. *Science* **281**, 200–206 (1998).
2. Siegel, D. A. et al. Global assessment of ocean carbon export by combining satellite observations and food-web models. *Global Biogeochem. Cycles* **28**, 181–196 (2014).
3. Henson, S., Le Moigne, F. & Giering, S. Drivers of carbon export efficiency in the global ocean. *Global Biogeochem. Cycles* **33**, 891–903 (2019).
4. Buesseler, K. O., Boyd, P. W., Black, E. E. & Siegel, D. A. Metrics that matter for assessing the ocean biological carbon pump. *Proc. Natl Acad. Sci. USA* **117**, 9679–9687 (2020).
5. Henson, S. A. et al. Uncertain response of ocean biological carbon export in a changing world. *Nat. Geosci.* **15**, 248–254 (2022).
6. Sallée, J.-B. et al. Summertime increases in upper-ocean stratification and mixed-layer depth. *Nature* **591**, 592–598 (2021).
7. Doney, S. C. Plankton in a warmer world. *Nature* **444**, 695–696 (2006).
8. Boyd, P. W. et al. Marine phytoplankton temperature versus growth responses from polar to tropical waters – outcome of a scientific community-wide study. *PLoS ONE* **8**, e63091 (2013).
9. Dutkiewicz, S., Scott, J. R. & Follows, M. J. Winners and losers: ecological and biogeochemical changes in a warming ocean. *Global Biogeochem. Cycles* **27**, 463–477 (2013).
10. Behrenfeld, M. J. et al. Revaluating ocean warming impacts on global phytoplankton. *Nat. Clim. Change* **6**, 323–330 (2016).
11. Tagliabue, A. 'Oceans are hugely complex': modelling marine microbes is key to climate forecasts. *Nature* **623**, 250–252 (2023).
12. Groom, S. B. et al. Satellite ocean colour: current status and future perspective. *Front. Mar. Sci.* **6**, 485 (2019).
13. Zaneveld, J. R. V., Barnard, A. H. & Boss, E. Theoretical derivation of the depth average of remotely sensed optical parameters. *Opt. Express* **13**, 9052–9061 (2005).
14. Cullen, J. J. Subsurface chlorophyll maximum layers: enduring enigma or mystery solved? *Annu. Rev. Mar. Sci.* **7**, 207–239 (2015).
15. Cornec, M. et al. Deep chlorophyll maxima in the global ocean: occurrences, drivers and characteristics. *Glob. Biogeochem. Cycles* **35**, e2020GB006759 (2021).
16. Zhuang, Y. et al. Phytoplankton community structure at subsurface chlorophyll maxima on the western Arctic shelf: patterns, causes, and ecological importance. *J. Geophys. Res. Biogeosci.* **125**, e2019JG005570 (2020).
17. Arteaga, L. A., Behrenfeld, M. J., Boss, E. & Westberry, T. K. Vertical structure in phytoplankton growth and productivity inferred from biogeochemical-Argo floats and the carbon-based productivity model. *Glob. Biogeochem. Cycles* **36**, e2022GB007389 (2022).
18. Bouman, H. A., Jackson, T., Sathyendranath, S. & Platt, T. Vertical structure in chlorophyll profiles: influence on primary production in the Arctic Ocean. *Philos. Trans. R. Soc. A* **378**, 20190351 (2020).
19. Cox, I. et al. Distinct habitat and biogeochemical properties of low-oxygen-adapted tropical oceanic phytoplankton. *Limnol. Oceanogr.* **68**, 2022–2039 (2023).
20. Brewin, R. J. W. et al. A conceptual approach to partitioning a vertical profile of phytoplankton biomass into contributions from two communities. *J. Geophys. Res. Oceans* **127**, e2021JC018195 (2022).
21. Hu, Q. et al. Seasonal variability of phytoplankton biomass revealed by satellite and BGC-Argo data in the central tropical Indian Ocean. *J. Geophys. Res. Oceans* **127**, e2021JC018227 (2022).
22. Ross, T. et al. Blooms and subsurface phytoplankton layers on the Scotian shelf: insights from profiling gliders. *J. Mar. Syst.* **172**, 118–127 (2017).
23. Bittig, H. C. et al. A BGC-Argo guide: planning, deployment, data handling and usage. *Front. Mar. Sci.* **6**, 502 (2019).
24. Lomas, M. W., Bates, N. R., Johnson, R. J., Steinberg, D. K. & Tanioka, T. Adaptive carbon export response to warming in the Sargasso Sea. *Nat. Commun.* **13**, 1211 (2022).
25. D'Alelio, D. et al. Machine learning identifies a strong association between warming and reduced primary productivity in an oligotrophic ocean gyre. *Sci. Rep.* **10**, 3287 (2020).
26. Lomas, M. W. et al. Two decades and counting: 24-years of sustained open ocean biogeochemical measurements in the Sargasso Sea. *Deep Sea Res. Pt. II* **93**, 16–32 (2013).
27. Moeller, H. V., Laufkötter, C., Sweeney, E. M. & Johnson, M. D. Light-dependent grazing can drive formation and deepening of deep chlorophyll maxima. *Nat. Commun.* **10**, 1978 (2019).
28. Lomas, M. W. et al. Varying influence of phytoplankton biodiversity and stoichiometric plasticity on bulk particulate stoichiometry across ocean basins. *Commun. Earth Environ.* **2**, 143 (2021).
29. Baer, S. E., Lomas, M. W., Terpis, K. X., Mouginot, C. & Martiny, A. C. Stoichiometry of *Prochlorococcus*, *Synechococcus*, and small eukaryotic populations in the western North Atlantic Ocean. *Environ. Microbiol.* **19**, 1568–1583 (2017).
30. Sathyendranath, S. et al. Carbon-to-chlorophyll ratio and growth rate of phytoplankton in the sea. *Mar. Ecol. Prog. Ser.* **383**, 73–84 (2009).
31. Flynn, K. J. et al. Acclimation, adaptation, traits and trade-offs in plankton functional type models: reconciling terminology for biology and modelling. *J. Plankton Res.* **37**, 683–691 (2015).
32. Osborn, T. J. Winter 2009/2010 temperatures and a record-breaking North Atlantic Oscillation index. *Weather* **66**, 19–21 (2011).
33. Zhang, R. Anticorrelated multidecadal variations between surface and subsurface tropical North Atlantic. *Geophys Res. Lett.* **34**, L12713 (2007).
34. Zhang, R. et al. Have aerosols caused the observed Atlantic multidecadal variability? *J. Atmos. Sci.* **70**, 1135–1144 (2013).
35. Frajka-Williams, E., Beaulieu, C. & Duchez, A. Emerging negative Atlantic multidecadal oscillation index in spite of warm subtropics. *Sci. Rep.* **7**, 11224 (2017).
36. Trenberth, K., Zhang, R. & National Center for Atmospheric Research (NCAR) Staff. Atlantic multi-decadal oscillation (AMO) and Atlantic multidecadal variability (AMV). *NCAR* https://climatedataguide.ucar.edu/climate-data/atlantic-multi-decadal-oscillation-amo (2024).
37. Sathyendranath, S. et al. An ocean-colour time series for use in climate studies: the experience of the Ocean-colour Climate Change Initiative (OC-CCI). *Sensors* **19**, 4285 (2019).
38. van Oostende, M., Hieronymi, M., Krasemann, H. & Baschek, B. Global ocean colour trends in biogeochemical provinces. *Front. Mar. Sci.* **10**, 781 (2023).
39. Brewin, R. J. W. et al. Sensing the ocean biological carbon pump from space: a review of capabilities, concepts, research gaps and future developments. *Earth Sci. Rev.* **217**, 103604 (2021).
40. Brewin, R. J. W. et al. Ocean carbon from space: current status and priorities for the next decade. *Earth Sci. Rev.* **240**, 104386 (2023).
41. Chai, F. et al. Monitoring ocean biogeochemistry with autonomous platforms. *Nat. Rev. Earth Environ.* **1**, 315–326 (2020).

42. Roemmich, D. et al. On the future of Argo: a global, full-depth, multi-disciplinary array. *Front. Mar. Sci.* **6**, 436860 (2019).
43. Claustre, H., Johnson, K. S. & Takeshita, Y. Observing the global ocean with biogeochemical-Argo. *Annu. Rev. Mar. Sci.* **12**, 23–48 (2020).
44. Behrenfeld, M. J. et al. Satellite lidar measurements as a critical new global ocean climate record. *Remote Sens.* **15**, 5567 (2023).
45. Dai, M. et al. Upper ocean biogeochemistry of the oligotrophic North Pacific subtropical gyre: from nutrient sources to carbon export. *Rev. Geophys.* **61**, e2022RG000800 (2023).

Methods

Data processing

The BATS data used in this study were acquired freely from the BATS data server (http://bats.bios.edu/bats-data/) for Niskin bottle data and the BATS project page at the Biological-Chemical Oceanography Data Management Office (https://www.bco-dmo.org/project/2124) for high-performance liquid chromatography (HPLC) pigment and CTD data. Three BATS datasets were downloaded: CTD casts, discrete Niskin bottle measurements and in situ pigment measurements including HPLC Chl-*a*. From this unique long-term BATS dataset, we constructed a 33-year-long time series of CTD, pigment and bottle vertical profile data (monthly to biweekly in spring) from January 1990 to December 2022. Only profiles within a 0.5° latitude by longitude box (0.25° margin) around the BATS site were used for this study (Supplementary Fig. 5). From the CTD data, we extracted temperature and salinity from which to calculate density, mixed-layer depth and the Brunt–Väisälä buoyancy frequency (BVF). From the pigment data, HPLC Chl-*a* concentrations were extracted, and from the bottle data, POC concentrations were extracted. Detailed information on the sampling, analysis and quality of the CTD, HPLC and POC data can be found in the BATS methods manual[46] and previous studies[26,47].

For the CTD data, only casts were included where both temperature and salinity measurements were available and where temperature measurements were available in the upper 11 m. For the Chl-*a* profiles, only those with at least six bottle measurements with coincident CTD and POC profiles were included in this study. For the POC profiles, an outlier analysis was performed to remove spikes using a modified *z* score, based on a moving median and the median absolute deviation, where data with a *z* score greater than 3 were removed. The resulting dataset contained a total of 416 Chl-*a* and POC profiles that could be used to fit a modified version of the Brewin et al.[20] two-community model, as described below. The monthly and annual sampling distributions of the profiles used in this study are shown in Supplementary Tables 2–4 and Supplementary Fig. 6.

The euphotic depth (Z_p) was estimated for each Chl-*a* profile using the algorithm from ref. 48, with the surface Chl-*a* concentration as the input. The diffuse attenuation coefficient (K_d) for photosynthetically available radiation (PAR) was then taken to be $4.6/Z_p$. The K_d based on the PAR was not directly computed in this study due to the low availability of CTD profiles with PAR data that corresponded to Chl-*a* profiles. The density and BVF were computed for each CTD profile using the Python seawater package[49]. The MLD was computed for each CTD profile from the temperature using the temperature MLD algorithm from ref. 50 in the holteandtalley Python package. The temperature MLD was used rather than density to compare the results to a recent BATS study[24] that also used a temperature algorithm. Daily average satellite PAR values for BATS were derived from Moderate Resolution Imaging Spectroradiometer (MODIS) 8-day composite data (2002–2022), taking the median daily PAR of 3 × 3 pixels from around the BATS location (Data Availability). To estimate light levels in the mixed layer, the average mixed-layer irradiance was computed from the satellite surface PAR, in situ estimates of K_d and MLD (see equation (11) in ref. 51). The irradiance levels experienced by the subsurface phytoplankton were estimated by propagating the surface satellite PAR to the DCM depth using the Beer–Lambert law and in situ estimates of K_d. For each calculation, 2% was subtracted from the above-water-surface PAR to derive the below-water-surface PAR, to account for the light lost via reflection at the ocean surface. To assess some aspects of the phytoplankton community composition, other HPLC pigment data (not only HPLC Chl-*a*) were also analysed in samples from BATS, where zeaxanthin and lutein could be separated, to calculate the photoprotective photo-pigment indices and diagnostic pigment ratios for phytoplankton functional groups, based on ref. 52.

Partitioning of a phytoplankton biomass vertical profile into two communities

We applied an adapted version of the Brewin et al.[20] model to the long-term BATS time series of coincident Chl-*a* and POC concentration profiles. The approach was designed to partition the vertical profiles of Chl-*a* into two phytoplankton communities—a surface community that predominantly resides in the surface mixed layer, described using a sigmoid function, and a subsurface community living below the mixed layer, described using a Gaussian function. Brewin et al.[20] provided a detailed explanation of the theoretical background and model fitting steps, along with the mathematical functions used and example code for the model. Here we describe how the Brewin et al.[20] model was adapted to Chl-*a* and POC from the BATS time series (see Supplementary Fig. 7 for an example fit).

Chlorophyll model fitting. The Chl-*a* model is fitted by first deriving the dimensionless optical depth (τ), computed by multiplying K_d (m^{-1}) by the geometric depth (m), and then normalizing the Chl-*a* profile (B) using its surface (measurement closest to the surface in the profile) concentration (B_s). The normalized Chl-*a* profile (B^*) at a given optical depth (τ) is then expressed as

$$B^*(\tau) = 1 - \frac{1}{1+\exp\left[-\frac{P_1}{\tau_1}(\tau-\tau_1)\right]} + B^*_{m,2}\exp\left\{-\left[(\tau-\tau_2)/\sigma\right]^2\right\}. \quad (1)$$

Community 1 (surface, B^*_1) is represented by the first term on the right-hand side of equation (1), where P_1 relates to the slope in B^*_1 and τ_1 is the mid-point of the slope. Community 2 (subsurface, B^*_2) is represented by the second term on the right-hand side of equation (1), where $B^*_{m,2}$ is the maximum value at the DCM, τ_2 is the depth of the DCM and σ is the width of the DCM. Once the model parameters have been derived after the optimization, the modelled Chl-*a* profiles can be reconstructed by scaling the dimensionless profiles by the surface Chl-*a* and K_d, such that Chl-*a* (B) at depth (z) can be expressed as

$$B(z) = B_1(z) + B_2(z) \quad (2)$$

where B_1 is the Chl-*a* concentration of community 1 (surface) and B_2 is the Chl-*a* concentration of community 2 (subsurface).

Particulate organic carbon model fitting. We extended the Brewin et al.[20] model to the coincident profiles of POC concentration by deriving a fixed carbon-to-chlorophyll ratio (C:Chl) per community for each profile, and assuming a fixed background carbon of non-algal particles for each profile (see Supplementary Section 4.3 for validation). We first normalized the POC profile by dividing it by the surface POC, taken to be the median POC in the first optical depth ($1/K_d$). This method is similar to the extension of the model for particle backscattering profiles in ref. 20. The normalized POC (POC^*) at a given optical depth can be considered as a combination of the two communities and a non-algal component, expressed as

$$\mathrm{POC}^*(\tau) = \varphi_1 B^*_1(\tau) + \varphi_2 B^*_2(\tau) + C^*_N. \quad (3)$$

Here, φ_1 and φ_2 are scaling factors linking the two communities of phytoplankton to the POC, and C^*_N is the constant background non-algal carbon factor. Following Brewin et al.'s extension of the model for particle backscattering[20], we assume φ_1 can be expressed as $1 - C^*_N$, such that the normalized POC model can be expressed as

$$\mathrm{POC}^*(\tau) = (1 - C^*_N)B^*_1(\tau) + \varphi_2 B^*_2(\tau) + C^*_N. \quad (4)$$

Once the model parameters are known, the modelled POC profiles can be reconstructed by scaling the normalized profiles by the surface POC and K_d. Ultimately, the POC model can be expressed as

$$\mathrm{POC}(z) = C^B_1 B_1(z) + C^B_2 B_2(z) + C_N, \quad (5)$$

and

$$\mathrm{POC}(z) = C_1(z) + C_2(z) + C_N, \quad (6)$$

where C_1 is the carbon concentration of community 1 (surface), C_2 is the carbon concentration of community 2 (subsurface) and C_N is the carbon of the non-algal particles.

Model parameterization, fitting and optimization. To fit and parameterize the Chl-*a* model, a similar process was followed to that of Brewin et al.[20], as described above, using nonlinear optimization (Python lmfit.minimize using the powell method), but with the addition of a third step to improve the parameters of the surface community in cases where a DCM was present, by utilizing the shape of the POC profile. In this third step, for profiles where both communities were present (sigmoid equation explaining <90% of the variance of the Chl-*a* profile), the POC model was fitted, initially, using the method of Brewin et al.[20] to temporarily derive the φ_1 and φ_2 scaling factors. The POC model was then fitted again, but these scaling factors, and the parameters for the subsurface community, were fixed from the previous steps, and the τ_1 parameter for the surface community was allowed to vary (P_1 was tied to τ_1, as in ref. 20). This resulted in an improved estimation of the depth of the slope of the sigmoid function (τ_1) for the BATS site in the presence of a DCM, instead of relying on the regional Red Sea relationship between τ_1 and the MLD multiplied by K_d, as in ref. 20. The Chl-*a* model was then refitted using the newly optimized τ_1 and P_1 values, allowing the parameters for the subsurface Gaussian function to vary.

Having derived $B_1^*(\tau)$ and $B_2^*(\tau)$ using the model fitted to the Chl-*a* profiles, C_N^* and φ_2 were estimated using nonlinear optimization (Python lmfit.minimize using the powell method). The initial guesses for C_N^* and φ_2 were set to 0.2 and 0.3, respectively, and were constrained to a lower limit of 0.01 and an upper limit of 0.95. Once φ_2 and C_N^* were known, the C:Chl ratio for each community (C_1^B and C_2^B) was derived by dividing the scaling factors for each community (φ_1 and φ_2) by the ratio of the surface Chl-*a* and surface POC. The non-algal component of POC, C_N, was computed by multiplying C_N^* by the surface POC. For the POC profiles, depths down to 400 m were included, where available, to improve the estimate of C_N by including POC concentrations from well below the euphotic depth and below 250 m, where phytoplankton rarely grow[14]. A time series of model parameters is shown in the Supplementary Fig. 8, as well as comparisons between the model results and the data (Extended Data Figs. 7a and 9a and Supplementary Figs. 10–13). The Python code used to tune the modified model to discrete bottle measurements of Chl-*a* and POC is freely available on GitHub (https://github.com/jjviljoen/Two-community-phyto-model-updated) and Zenodo[53].

Data analysis

The depth integration of the variables was carried out on each profile, from the surface to 1.5 times the Z_p (where Z_p represents the 1% light level and 1.5 times Z_p is 6.9 optical depths) using the trapezoid method[54] in Python (scipy.integrate.trapz). This approach is based on previous Chl-*a* modelling studies and accounts for the phytoplankton biomass often found below the Z_p[55–57]. Similarly, the average BVF from the surface to 1.5 times the Z_p was selected as an index of stratification for the region[58].

Long-term trends were explored by applying a trend analysis to various column-integrated raw and modelled results to remove seasonal patterns and extract long-term trends. De-seasonalized data were extracted using a seasonal decomposition analysis using the Python function MSTL from the statsmodels.tsa.seasonal package, with a period of 12 representing the months of the year. The data were resampled to a monthly time step (that is, a monthly median), and any month without data was filled with the climatological median of the month to keep the detection of seasonal patterns consistent during the analysis. Subsequently, linear regression analysis (Python sklearn.linear_model.LinearRegression) was applied to the integrated and extracted trend data to test whether the variables changed significantly (two-sided Pearson *P* value) over the entire time series and shorter time periods. For the linear trend analysis, 1 January 2011 was used as the inflection point, based on observations by Lomas et al.[24]. We further justified the selection objectively by using two different change point detection methods—the second derivative method and the Dynp function from the ruptures Python package—that searched for single inflection points using our SST observations (which ranged between 2010 and 2013). SST was used for inflection point analysis, being a single variable that represented various influences of climate variability. The relationship between the AMO index and the de-seasonalized data was determined via Spearman's correlation coefficient (*R*) and significance (*P*).

Data availability

BATS data used in this study were acquired freely from the BATS data server (http://bats.bios.edu/bats-data/) and the BATS project page at the Biological-Chemical Oceanography Data Management Office (https://www.bco-dmo.org/project/2124). Atlantic Meridional Oscillation index data used in this study were downloaded from NCAR's climate data guide (https://climatedataguide.ucar.edu/climate-data/atlantic-multi-decadal-oscillation-amo). Satellite MODIS 8-day composite PAR data were downloaded from the NASA ocean colour page (https://oceancolor.gsfc.nasa.gov/resources/atbd/par/). Two-community model data output of modelled Chl-*a* and POC vertical profiles are available via Zenodo at https://doi.org/10.5281/zenodo.13150754 (ref. 53).

Code availability

Python code used to process the BATS data and fit the modified two-community model to profiles of Chl-*a* and POC data is openly available on GitHub (https://github.com/jjviljoen/Two-community-phyto-model-updated) and via Zenodo at https://doi.org/10.5281/zenodo.13150754 (ref. 53).

References

46. Cruise information. *BATS* https://bats.bios.edu/about/cruise-information/ (2020).
47. Steinberg, D. K. et al. Overview of the US JGOFS Bermuda Atlantic Time-series Study (BATS): a decade-scale look at ocean biology and biogeochemistry. *Deep Sea Res. Pt. II* **48**, 1405–1447 (2001).
48. Morel, A. et al. Examining the consistency of products derived from various ocean color sensors in open ocean (Case 1) waters in the perspective of a multi-sensor approach. *Remote Sens. Environ.* **111**, 69–88 (2007).
49. Fofonoff, N. P. & Millard Jr, R. C. Algorithms for the computation of fundamental properties of seawater. *UNESCO Technical Papers in Marine Sciences* **44**, 1–53 (1983).
50. Holte, J. & Talley, L. A new algorithm for finding mixed layer depths with applications to Argo data and subantarctic mode water formation. *J. Atmos. Ocean Technol.* **26**, 1920–1939 (2009).
51. Brewin, R. J. W. et al. Influence of light in the mixed-layer on the parameters of a three-component model of phytoplankton size class. *Remote Sens. Environ.* **168**, 437–450 (2015).
52. Aiken, J. et al. Phytoplankton pigments and functional types in the Atlantic Ocean: a decadal assessment, 1995–2005. *Deep Sea Res. Pt. II* **56**, 899–917 (2009).
53. Viljoen, J. J., Sun, X. & Brewin, R. J. W. Model code and output for: Climate variability shifts the vertical structure of phytoplankton in the Sargasso Sea. *Zenodo* https://doi.org/10.5281/zenodo.13150754 (2024).
54. Ossendrijver, M. Ancient Babylonian astronomers calculated Jupiter's position from the area under a time-velocity graph. *Science* **351**, 482–484 (2016).
55. Uitz, J., Claustre, H., Morel, A. & Hooker, S. B. Vertical distribution of phytoplankton communities in open ocean: an assessment based on surface chlorophyll. *J. Geophys. Res. Oceans* **111**, 8005 (2006).

56. Brewin, R. J. W. et al. Modelling size-fractionated primary production in the Atlantic Ocean from remote sensing. *Prog. Oceanogr.* **158**, 130–149 (2017).
57. Saba, V. S. et al. Challenges of modeling depth-integrated marine primary productivity over multiple decades: a case study at BATS and HOT. *Global Biogeochem. Cycles* **24**, GB3020 (2010).
58. Jacket, D. R. & Mcdougall, T. J. Minimal adjustment of hydrographic profiles to achieve static stability. *J. Atmos. Ocean. Technol.* **12**, 381–389 (1995).
59. Westberry, T. K. et al. Annual cycles of phytoplankton biomass in the subarctic Atlantic and Pacific Ocean. *Global Biogeochem. Cycles* **30**, 175–190 (2016).

Acknowledgements

We sincerely thank and acknowledge all the researchers, technicians and data managers who contributed to the BATS site for the profound wealth of data produced since sampling started. Our work was supported by a UK Research and Innovation Future Leader Fellowship (MR/V022792/1) awarded to R.J.W.B. We thank E. Keall for his work as an undergraduate student, which helped inform the design of the study, D. Raitsos for suggesting the use of cumulative sums for some of the analysis (Supplementary Information), acknowledge useful discussions with G. Dall'Olmo that helped support the work, and we thank R. Zhang for insights regarding the use of the AMO index to represent multidecadal climate variability.

Author contributions

R.J.W.B. and J.J.V. designed the study. J.J.V. conducted the analyses and wrote the first draft of the manuscript with input from R.J.W.B. X.S. contributed to the satellite data acquisition, presentation of data and created the map of the BATS profile locations. R.J.W.B. and X.S. contributed to discussions, manuscript review and editing. R.J.W.B. acquired the funding.

Competing interests

The authors declare no competing interests.

Additional information

Extended data is available for this paper at https://doi.org/10.1038/s41558-024-02136-6.

Supplementary information The online version contains supplementary material available at https://doi.org/10.1038/s41558-024-02136-6.

Correspondence and requests for materials should be addressed to Johannes J. Viljoen.

Peer review information *Nature Climate Change* thanks Xiaoyan Chen and the other, anonymous, reviewer(s) for their contribution to the peer review of this work.

https://doi.org/10.1038/s41558-024-02136-6

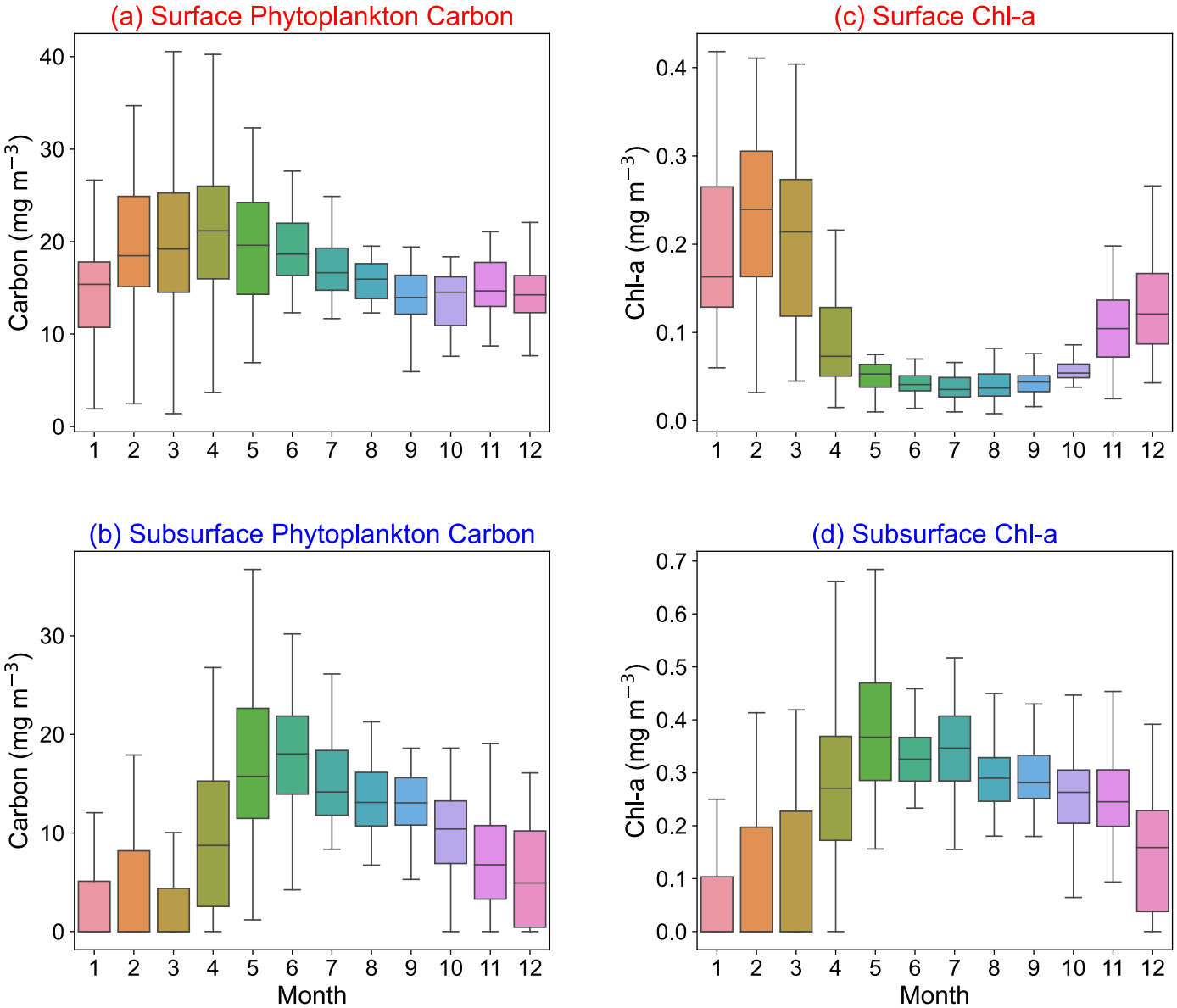

Extended Data Fig. 1 | Seasonality of surface and subsurface chlorophyll and phytoplankton carbon concentrations. Monthly boxplots of (**a**) surface and (**b**) subsurface phytoplankton carbon concentrations, (**c**) surface and (**d**) subsurface Chl-a concentrations at BATS. Surface concentrations are computed as the median value above the mixed layer depth (MLD) and subsurface concentrations as the value closest to the Deep Chlorophyll Maximum (DCM) depth (that is the maximum below the MLD). In all panels, the centre line is the median, boxes represent the interquartile range (25th to 75th percentiles), whiskers the 1.5x interquartile range. Outliers were removed to reduce the y-axis range of panels. See Fig. 1 for monthly boxplots of integrated stocks. See Table S3 for number of profiles and values per month used to calculate each boxplot.

https://doi.org/10.1038/s41558-024-02136-6

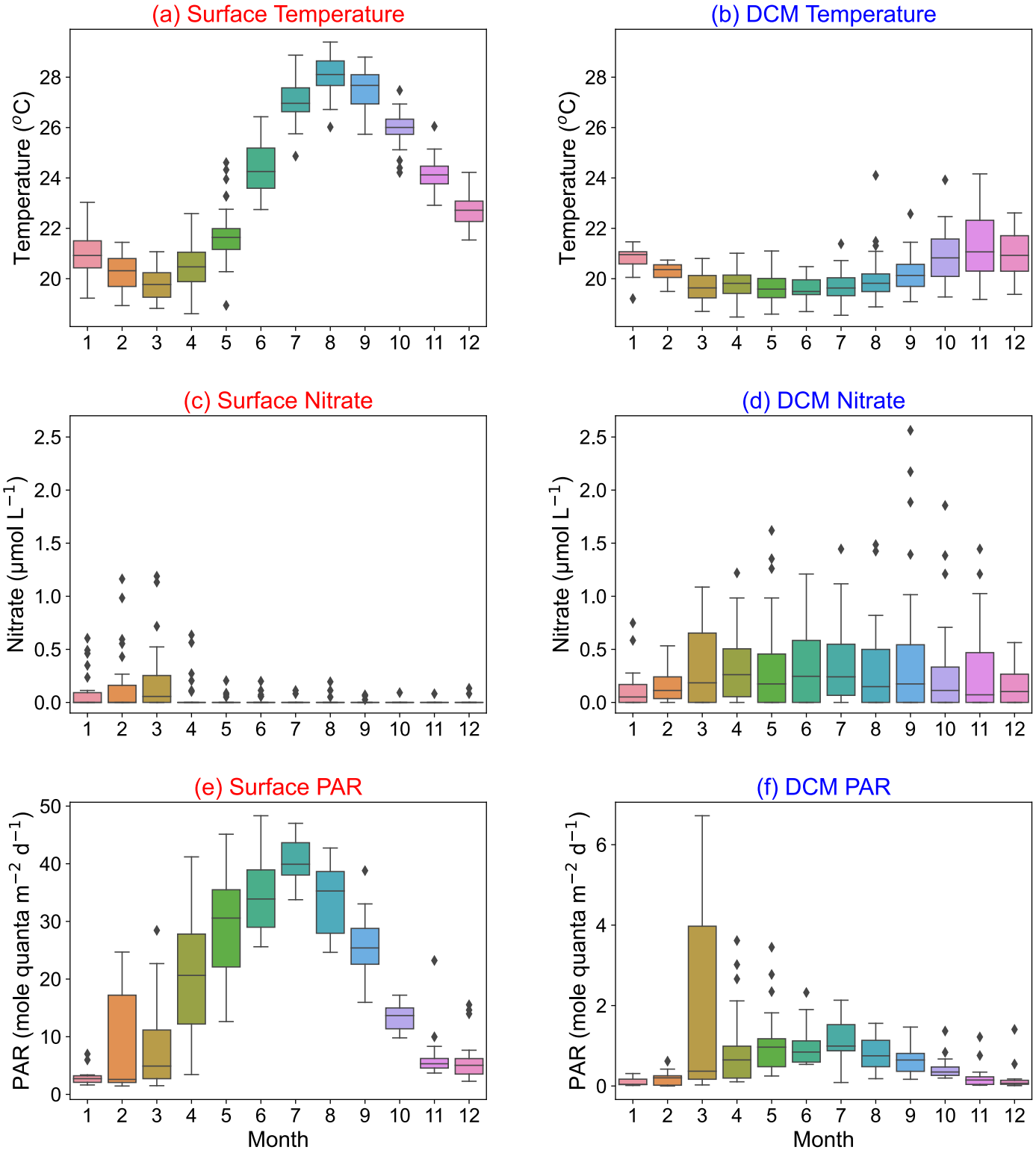

Extended Data Fig. 2 | Seasonality of temperature, nutrients and light experienced by surface and subsurface communities. Monthly boxplots of environmental conditions in the surface mixed layer (left) and below the MLD at the Deep Chlorophyll Maximum (DCM; right). For temperature (**a,b**) and nitrate (**c,d**), surface values are computed as the median value above the MLD and DCM is value closest to the DCM depth. (**e**) Surface Photosynthetically Available Radiation (PAR) is the estimated mean irradiance in the mixed layer computed from satellite derived PAR (see Methods). (**f**) The DCM PAR is estimated by propagating surface PAR to the DCM depth using Beer-lambert law and estimates of diffuse attenuation (Methods). In all panels, the centre line is the median, boxes represent the interquartile range (25th to 75th percentiles), whiskers the 1.5x interquartile range and points are outliers beyond this range. See Table S3 for number of profiles and values per month used to calculate each boxplot.

https://doi.org/10.1038/s41558-024-02136-6

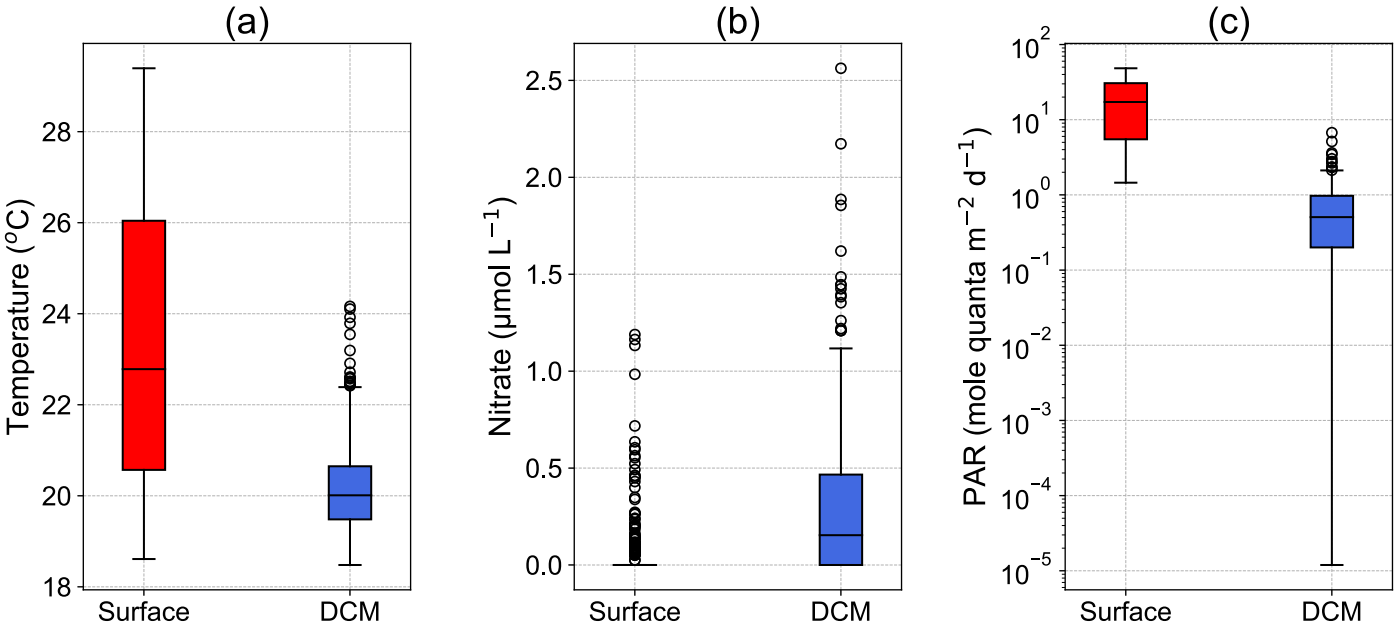

Extended Data Fig. 3 | Distinct environmental conditions of surface and subsurface phytoplankton. Boxplots of environmental conditions (**a**) Temperature, (**b**) Nitrate and (**c**) Photosynthetically Available Radiation (PAR), which the surface and subsurface communities inhabit. For temperature and nitrate, surface values are computed as the median value above the MLD and DCM is value closest to the DCM depth. Surface PAR is the estimated mean irradiance in the mixed layer computed from satellite derived PAR (see Methods). The DCM PAR is estimated by propagating surface satellite PAR to the DCM depth using Beer-lambert law and estimates of diffuse attenuation (see Methods). In all panels, the centre line is the median, boxes represent the interquartile range (25th to 75th percentiles), whiskers the 1.5x interquartile range and points are outliers beyond this range.

https://doi.org/10.1038/s41558-024-02136-6

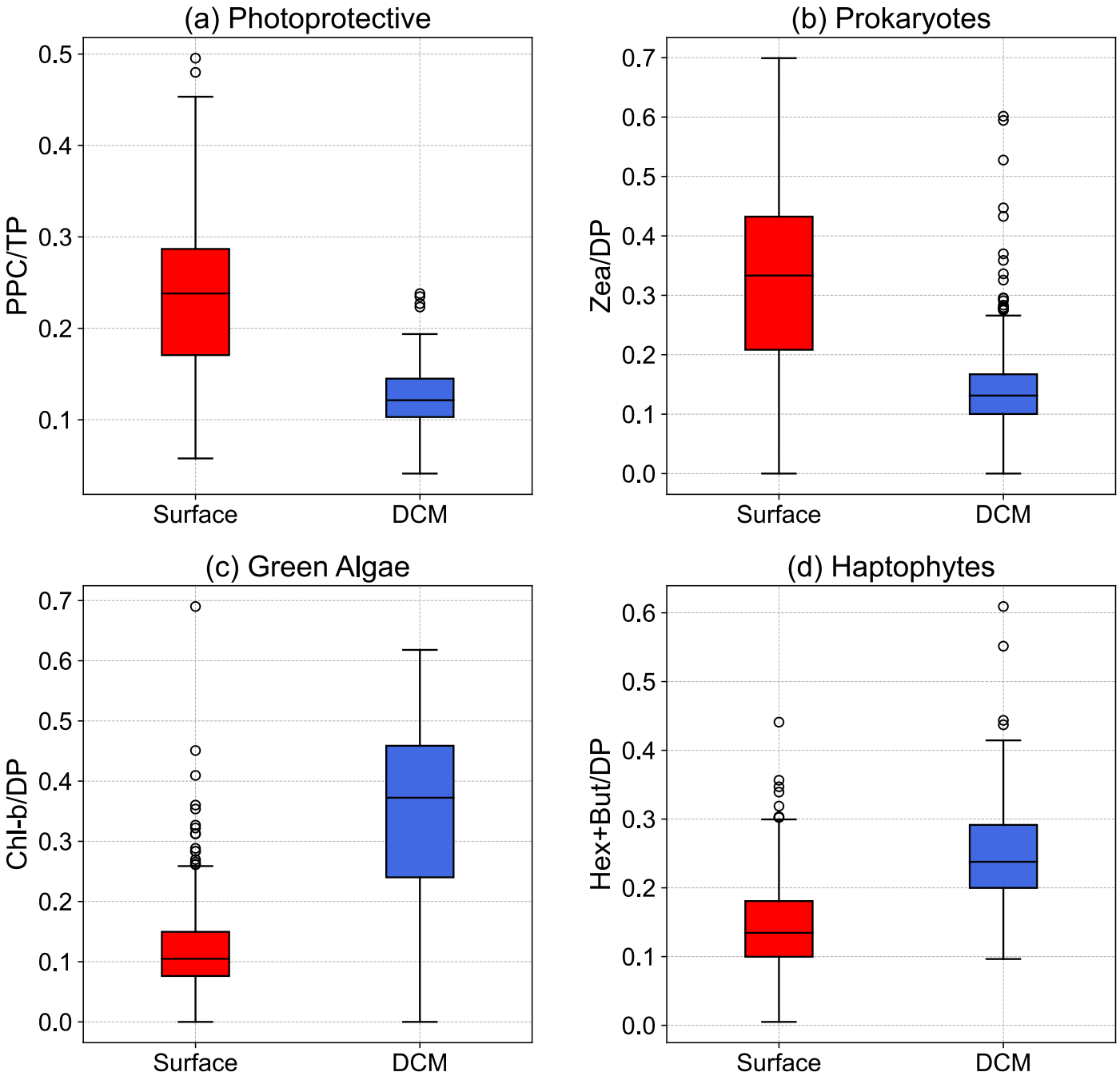

Extended Data Fig. 4 | Photoprotective and diagnostic pigments of surface and subsurface phytoplankton. Boxplots of (**a**) photoprotective photopigment indices and diagnostic pigment ratios of phytoplankton functional groups for (**b**) Prokaryotes, (**c**) Green Algae and (**d**) Haptophytes[52]. Surface values are computed as the median value above the mixed layer depth (MLD) and DCM is value closest to the Deep Chlorophyll Maximum depth. In all panels, the centre line is the median, boxes represent the interquartile range (25th to 75th percentiles), whiskers the 1.5x interquartile range and points are outliers beyond this range. Surface communities are dominated by prokaryotes and the subsurface by eukaryotes.

https://doi.org/10.1038/s41558-024-02136-6

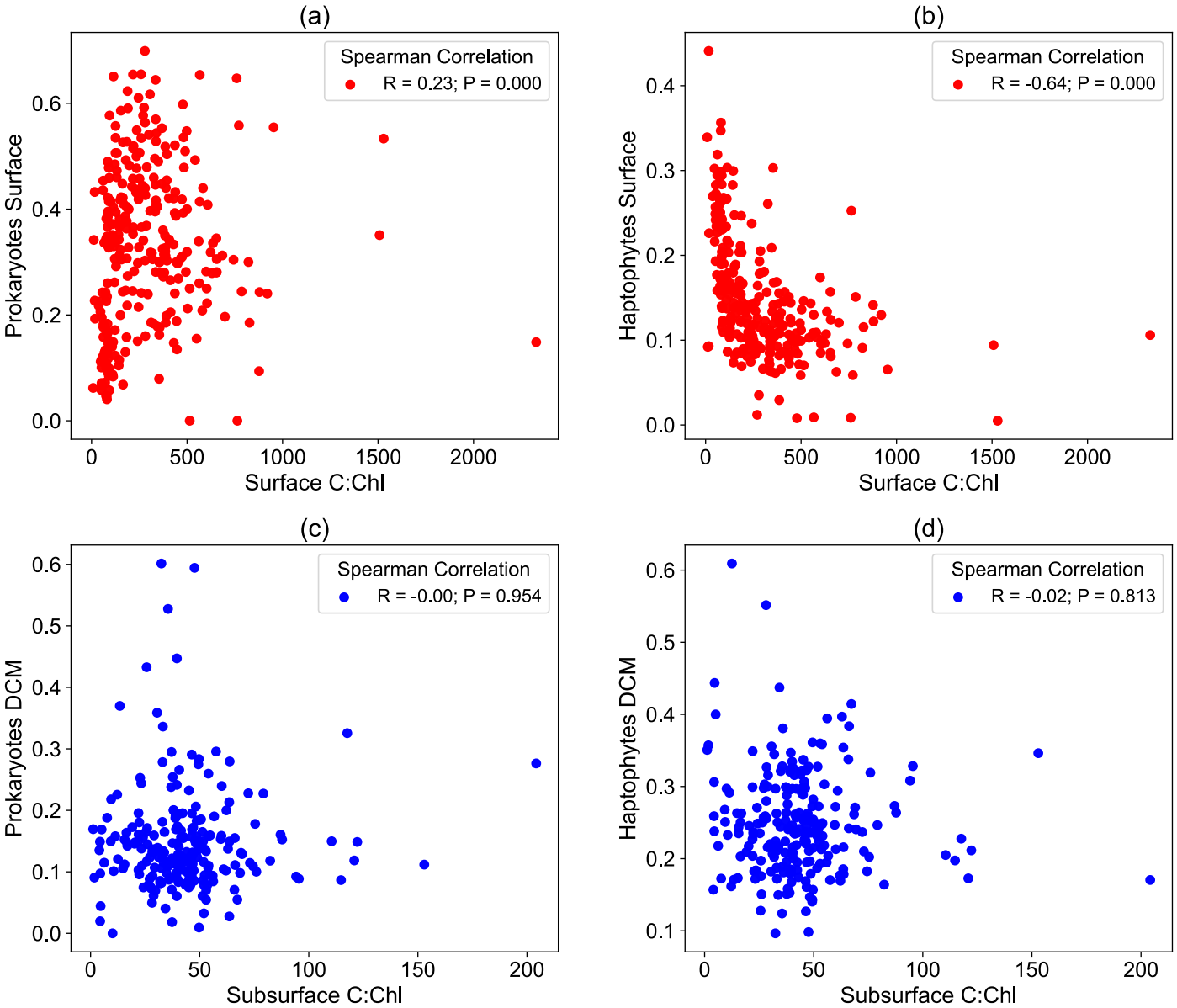

Extended Data Fig. 5 | Relationship between phytoplankton groups and carbon-to-chlorophyll ratios. Spearman correlation analysis between phytoplankton C:Chl and selected phytoplankton group proportion determined via diagnostic pigment ratios of phytoplankton functional groups for (**a,c**) Prokaryotes and (**b,d**) Haptophytes[52]. For Prokaryotes and Haptophytes, surface values are computed as the median value above the mixed layer depth (MLD) and DCM is value closest to the Deep Chlorophyll Maximum depth. Surface Prokaryotes and Haptophytes had a significant relationship with surface C:Chl (**a,b**), while no significant relationship is apparent with subsurface C:Chl. See Extended Data Fig. 4 for phytoplankton community composition comparison between the surface and the subsurface (DCM depth).

https://doi.org/10.1038/s41558-024-02136-6

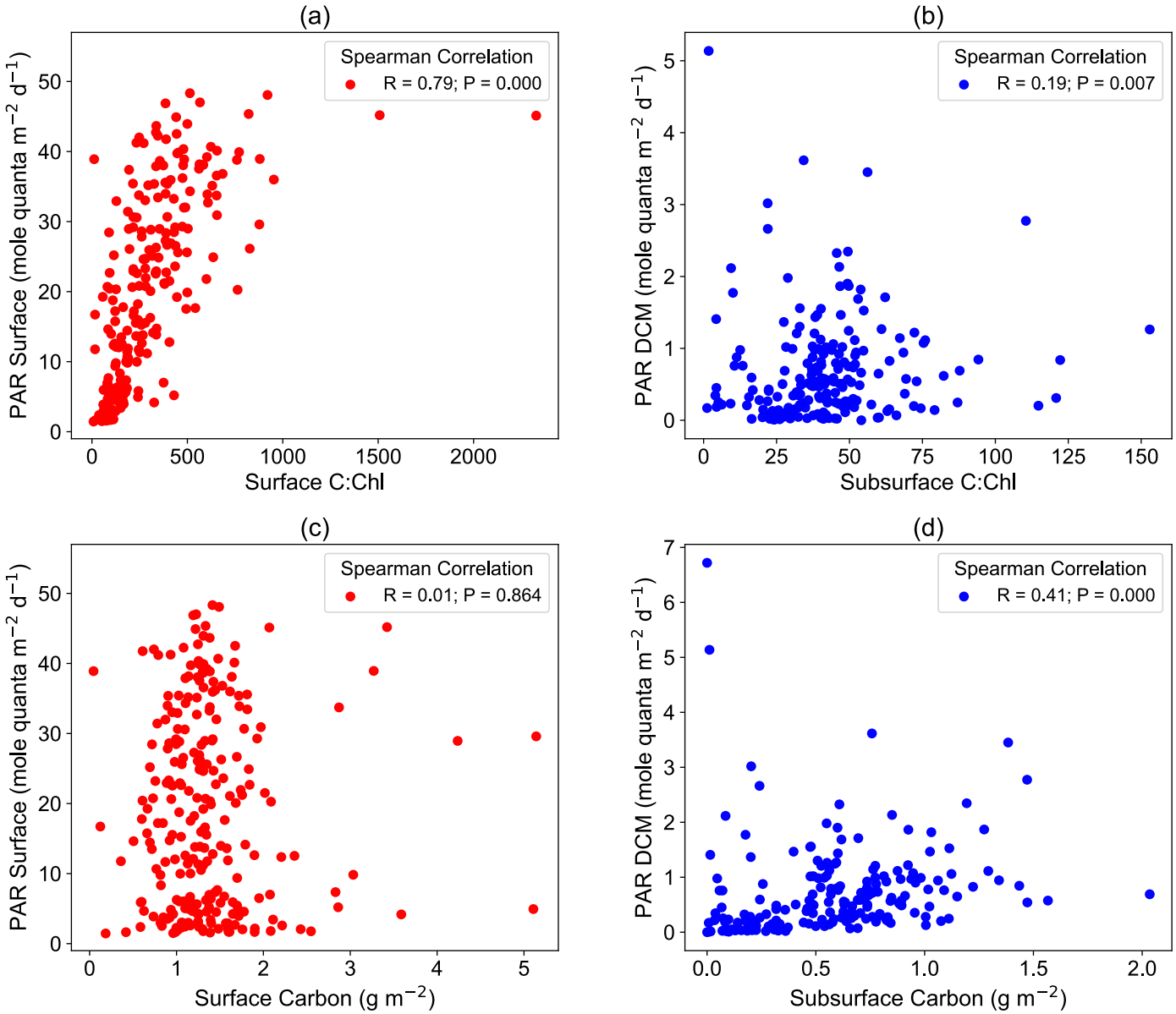

Extended Data Fig. 6 | Relationship between light levels, carbon-to-chlorophyll ratios, and phytoplankton carbon. a–**d**, Spearman correlation analysis of modelled phytoplankton (C:Chl (**a**,**b**) and carbon (**c**,**d**) of surface and subsurface communities compared to light levels in these two layers. Average light in the mixed layer was compared to the surface community and light at the Deep Chlorophyll Maximum (DCM) depth was compared to the subsurface community. The average Photosynthetically Available Radiation (PAR) for the surface community was computed as the average irradiance in the mixed layer from satellite derived PAR (see Methods). The DCM PAR was estimated by propagating surface satellite PAR to the DCM depth using the Beer-lambert law and estimates of diffuse attenuation (see Methods). Surface C:Chl ratio has a significant and strong relationship with the estimated mean light level in the in mixed layer (**a**), similar to Westberry et al.[59], while subsurface C:Chl has a significant but very weak relationship with light at the DCM (**b**). Instead, the light level (PAR) at the DCM has a stronger relationship with integrated subsurface carbon which is suggesting the subsurface shows a stronger biomass response (rather than change in C:Chl).

https://doi.org/10.1038/s41558-024-02136-6

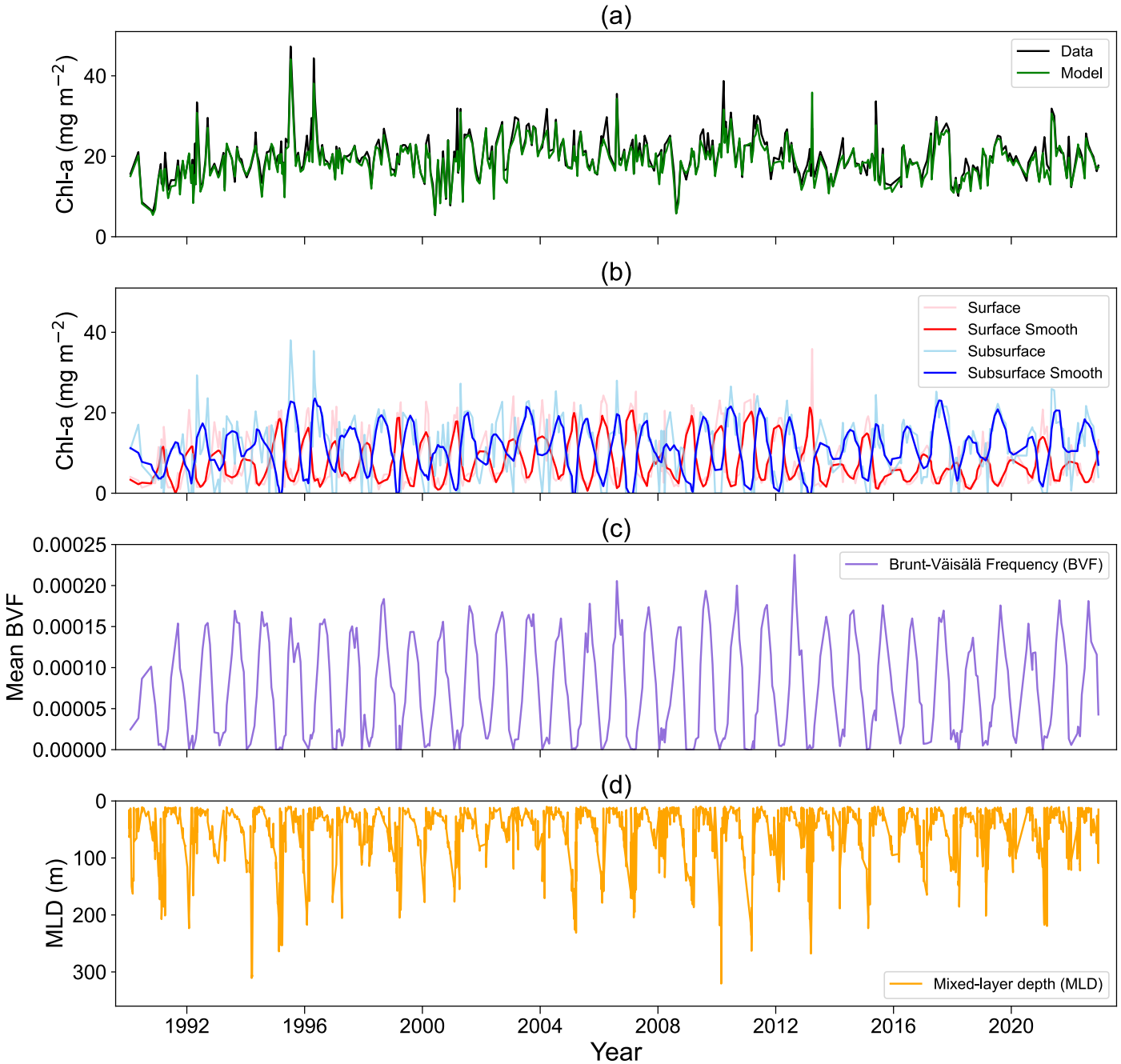

Extended Data Fig. 7 | Time series of total, surface and subsurface chlorophyll compared to stratification, and mixed-layer depth. (**a**) Integrated total Chl-a concentrations (mg m^{-2}) for data and model output. (**b**) Integrated surface and subsurface Chl-a concentrations (smoothed data computed using Python *savgol_filter* with a window size of 11, polyorder of 2 and nearest mode). Depth-integration done from the surface to 1.5 times the euphotic depth (1.5 x Z_p; see Methods). (**c**) Average Brunt-Väisälä buoyancy Frequency (BVF) index of stratification in 1.5 times Z_p. (**d**) Mixed-layer depth (MLD) from all CTD profiles included in the study (Max MLD of 321 m in February 2010). See Extended Data Fig. 8 for de-seasoned MLD time series and trend analysis. See Figure S12a for Spearman relationship between integrated Chl-a data and modelled Chl-a.

https://doi.org/10.1038/s41558-024-02136-6

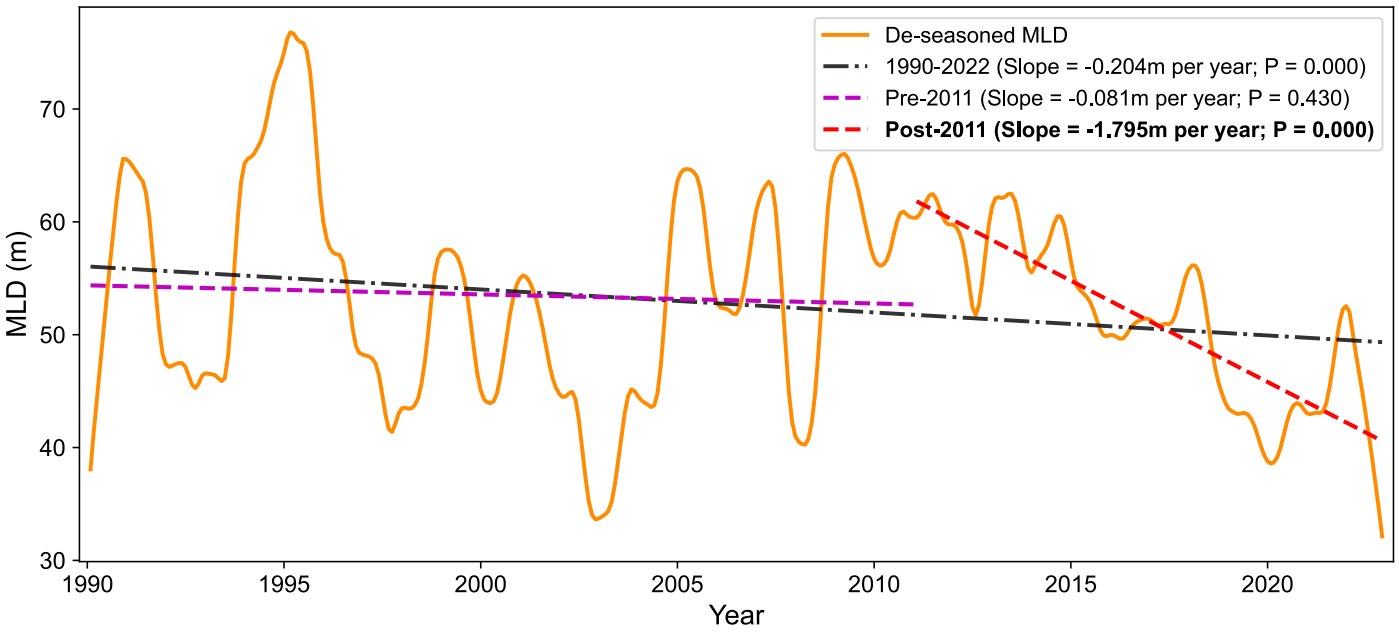

Extended Data Fig. 8 | Multidecadal decreasing mixed layer depth at BATS. Time series of de-seasoned Mixed-Layer Depth (MLD) data at BATS computed from CTD sensor temperature profiles included in the study (Methods). Solid orange line: de-seasoned MLD data. Dashed black line: is the linear regression applied to the entire de-seasoned MLD time series (1990–2022). Dashed purple line is the linear regression fitted to de-seasoned MLD up to the end of 2010 (Pre-2011; 1990–2010). Dashed red line is the linear regressions fitted to de-seasoned MLD only from 2011 up to the end of 2022 (Post-2011; 2011–2022). P = significance of the trends via Pearson correlation. See Data Analysis for extracting deseasonalised data and for details on the linear trend analysis (Methods). See Extended Data Fig. 7d for MLD time series.

https://doi.org/10.1038/s41558-024-02136-6

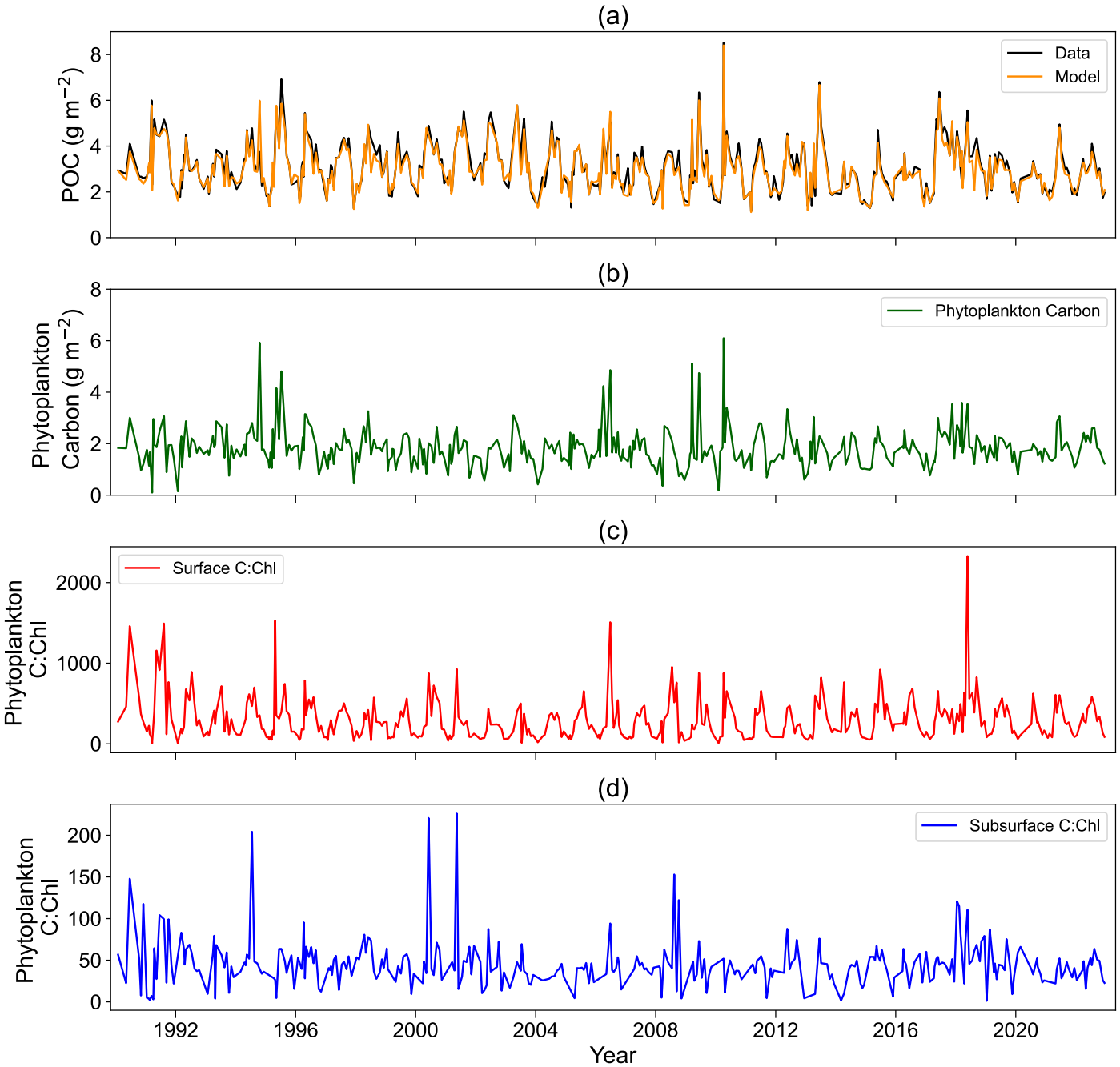

Extended Data Fig. 9 | Time series of particulate organic carbon, phytoplankton carbon and carbon-to-chlorophyll ratios. (**a**) Integrated total particulate organic carbon (POC) concentrations (g m^{-2}) for the data and model output. (**b**) Integrated phytoplankton carbon concentrations (g m^{-2}) from model output. Depth-integration done from the surface to 1.5 times the euphotic depth (1.5 x Z_p; Methods). Carbon-to-chlorophyll ratios (C:Chl) for (**c**) surface phytoplankton and (**d**) subsurface phytoplankton from model output. See Figure S12b for Spearman relationship between integrated POC data and integrated modelled POC.